Transport in Porous Media (2025) 152:34
https://doi.org/10.1007/s11242-025-02171-7

Differential Imaging-Based Porous Plate Measurements of Fluid Distribution and Capillary Pressure During Drainage in a Multiscale Oolitic Limestone

Anindityo Patmonoaji[1] · Rukuan Chai[1] · Asli S. Gundogar[1] · Mohamed Regaieg[2] · Martin J. Blunt[1] · Branko Bijeljic[1]

Received: 19 December 2024 / Accepted: 17 March 2025 / Published online: 16 April 2025

Abstract
Using a combination of a porous plate, micro-computed tomography, and differential imaging, the differential imaging porous plate (DIPP) method was employed to monitor spatial fluid distribution and measure capillary pressure between oil and water in an oolitic limestone, Ketton. Based on geological interpretation, mercury intrusion capillary pressure (MICP), and scanning electron microscopy (SEM), the pores were classified into macropores, intermediate-size pores, and micropores. Macropores are formed by the intergranular packing of ooid spheres, micropores are found within the intragranular porosity of the ooids, and intermediate-size pores arise from interstitial particles filling the macropores. This multiscale classification was validated by observing the fluid distribution patterns during drainage. A comparison with MICP showed that DIPP tends to yield lower capillary pressure values even after correction for fluid properties, consistent with previous studies on laminated sandstones. The results suggest that porous plate measurements using oil and water provide a more representative characterization of capillary pressure than MICP.

Keywords Capillary pressure · Drainage · Porous plate · Limestone · X-ray imaging

1 Introduction

Multiphase flow in porous media plays important roles in hydrogeology (Bear 1972; Blunt 2017), groundwater contamination and remediation (Jo et al. 2010; Hu and Xia 2018), carbon sequestration (Bashir et al. 2018), and geological hydrogen storage (Heinemann et al. 2021).

One of the most critical measurements is capillary pressure (Vavra et al. 1992), defined as the pressure difference across the interface between two immiscible fluids. Characterizing capillary pressure is essential for predicting fluid distribution (Porter

✉ Anindityo Patmonoaji
a.patmonoaji@imperial.ac.uk

1 Department of Earth Science and Engineering, Imperial College London, London, UK

2 TotalEnergies One Tech, Pau, France

et al. 2010), relative permeability (Cheng et al. 2024), and subsequent fluid displacement (Andersen 2020). The capillary pressure as a function of saturation can be obtained through various methods, including the porous plate method (Falode and Manuel 2014), mercury intrusion capillary pressure (MICP) (Jiao et al. 2020), and centrifuge methods (Ayappa et al. 1989). Each method has its own advantages and disadvantages.

Among these techniques, the porous plate method is regarded as the most reliable; however, it requires samples on the order of centimeters and can take months to complete the measurements. In contrast, MICP delivers results relatively quickly, often within days, but its representativeness can be questionable. This is due to the use of mercury in a vacuum rather than pairs of reservoir fluids, which prevents the generation of irreducible saturation. Additionally, the rapid measurement of MICP raises concerns about whether the injection time is adequate for mercury to penetrate smaller pore sizes effectively. The centrifuge method introduces a pressure gradient during centrifugation, which can lead to inaccuracies in measuring pressure differences. Despite these limitations, it is important to note that none of these methods provides a spatial fluid distribution within the sample, which is crucial for understanding the multiphase flow physics in multiscale porous media.

Over the past few decades, X-ray micro-computed tomography (micro-CT) has become a vital tool for visualizing multiphase flow in porous media (Patmonoaji et al. 2021; Porter et al. 2010) because it offers in situ imaging. However, since the pore sizes may range over several orders of magnitude, it is challenging to resolve all the pore structure while retaining a representative field of view. To address this challenge, Lin et al. (2016) incorporated differential imaging, originally used to assess saturation at the cm-scale (Akin and Kovscek 2003), into pore-scale visualization with micro-CT, thereby enabling the assessment of spatial fluid distribution without voxel size limitations. Therefore, by integrating micro-CT imaging with differential imaging and the porous plate method, a new capillary pressure measurement technique capable of monitoring spatial fluid distribution in any pore size was developed (Lin et al. 2017; Lin et al. 2021; Zhang et al. 2023), called differential imaging porous plate (DIPP). This method facilitates the measurement of capillary pressure functions and spatial fluid distributions without the constraints imposed by the micro-CT voxel size. Additionally, DIPP utilizes smaller sample sizes, on the order of millimeters rather than centimeters in conventional measurements, which significantly reduces measurement time from months to just a few weeks (Lin et al. 2017).

Earlier studies utilizing DIPP were conducted on multiscale porous media, specifically laminated sandstone, featuring throat size distributions spanning up to two orders of magnitude, from 100 microns to 1 micron, as measured by MICP (Lin et al. 2017). Comparisons between DIPP, the porous plate method, and MICP revealed that the capillary pressure functions obtained from DIPP and traditional porous plate measurements on larger samples were in agreement although both were consistently lower than those derived from MICP. This discrepancy was attributed to the parallel lamination of the sample with respect to the flow direction, which was suggested to pose access difficulties for MICP measurements.

In this work, we conduct capillary pressure measurements with DIPP on Ketton limestone, which is an oolitic limestone (Diaz and Eberli 2019; Harris and Diaz 2019), with a throat size distribution from MICP spanning up to four order of magnitudes from 10 nanometers to 100 micrometers. (1) We characterize a porous medium with four orders of magnitude variation in pore size, (2) monitor the displacement of multiphase flow distribution, and (3) compare the capillary pressure function obtained with DIPP to MICP.

2 Materials and Methods

2.1 Materials

Geologically, Ketton limestone was formed during the Middle Jurassic period (Hudson and Clements 2007). It is primarily composed of calcium carbonate and classified as an oolitic limestone that is composed of spherical grains known as ooids. These ooids are formed through the accumulation of calcium carbonate around a nucleus (Bruckmann 1721). The formation process begins with a tiny core or nucleus, which may be a small fragment of shell, a sand grain, or another type of debris. As these particles are rolled around by water currents, calcium carbonate precipitates from the water and coats the nucleus. The ooid gradually grows by adding layer upon layer of calcium carbonate, creating concentric rings around the core (Batchelor et al. 2018). Due to this formation mechanism, the centers of the ooids tend to be more porous. The spaces between the ooids are typically filled with interstitial particles and materials, which can be introduced during rock formation or later through diagenetic processes. Common interstitial particles include microcrystalline calcite (micrite), crystalline calcite (sparite), and small detrital particles such as fine sand or silt (Coogan 1970). The porosity of Ketton limestone arises from three primary sources: the interparticle space among ooids, the spaces between interstitial particles within the packing of the ooids, and the intraparticle porosity within the concentric rings of the ooids formed during precipitation.

In this work, a Ketton limestone sample with a diameter of 6 mm and a length of 24 mm was used. The measured porosity, determined using a helium porosimeter, was 0.239 ± 0.008, while the absolute permeability measured from the single-phase flow pressure difference was 2.27 ± 0.23 Darcy. The capillary pressure as a function of saturation and the derived throat diameter from MICP (Tanino and Blunt 2012) are presented in Fig. 1a. The capillary pressure and derived throat diameter exhibit three regions with different gradients: (a) a low gradient at a saturation of about 0.55–1.0, (b) a high gradient at a saturation of around 0.35–0.55, and (c) another low gradient at a saturation of approximately 0–0.35. A low gradient represents a large change in saturation with capillary pressure and hence a large volume associated with a given pore size.

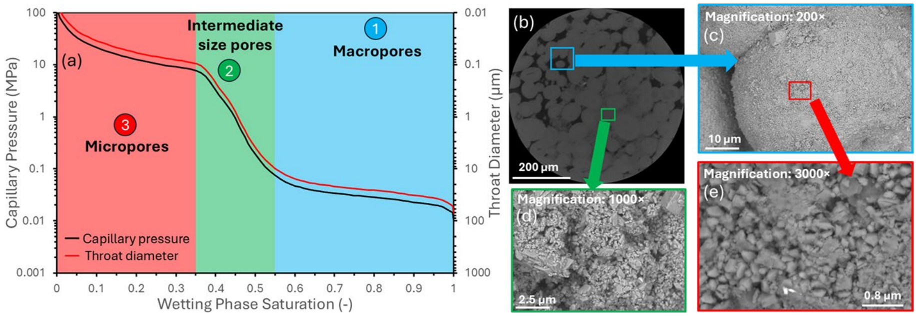

Fig. 1 **a** The capillary pressure function (black line) and the derived distribution of throat diameter of Ketton limestone from MICP (red line) (Tanino and Blunt 2012) with three characteristic categories: macropores (blue), intermediate-size pores (green), and micropores (red). **b** A two-dimensional cross-section of a three-dimensional micro-CT image and SEM images at different magnifications focusing on different characteristic categories of **c** macropores, **d** intermediate-size pores, and **e** micropores

Additionally, a cross-section obtained from micro-CT imaging is displayed in Fig. 1b, while microstructure images captured using a scanning electron microscope (SEM) are shown in Figs. 1c–e. With a magnification of 200×, the ooid sphere packing is visible (Fig. 1c), and at further 3000× magnification (Fig. 1e), the ooid surface also exhibits granular structure that comes from the precipitation process. The interstitial particle filling the ooid granular packing was also scanned with 1000× magnification and demonstrated crystal like structure with voids in between (Fig. 1d).

Based on the geological interpretation, MICP, and SEM observations, the pores are categorized into three groups: macropores (in the blue region), intermediate-size pores (in the green region), and micropores (in the red region), as illustrated in Fig. 1a. The macropores correspond to the spaces created by the intergranular packing of the ooid spheres, while the micropores refer to the intragranular pores of the ooid spheres resulting from mineralization and ooid formation. In contrast, intermediate-size pores represent the intergranular packing spaces filled by interstitial particles. According to the throat diameter derived from the MICP data, the throat size of macropores ranges from approximately 10 to 100 µm, intermediate-size pores range from 0.1 to 10 µm, and micropores range from 0.01 to 0.1 µm.

For the fluids, brine was prepared by doping deionized water with 30 wt% potassium iodide (KI), alongside decane. This doping concentration was determined to be optimal, as it provides significant contrast between decane, the solid matrix, and brine, while maintaining an acceptable X-ray attenuation value to prevent beam hardening (Lin et al. 2017; Lin et al. 2021; Zhang et al. 2023; Lin et al. 2016). The density and viscosity of the brine were measured as 1263 kg/m^3 and 0.82 mPa·s, respectively (Zhang et al. 2023). The non-wetting (oil) phase was decane (n-decane, Acros Organics) with density 730 kg/m^3, and viscosity 0.838 mPa·s (PubChem open chemistry database). The interfacial tension between brine and decane is 0.047 N/m (Zhang et al. 2023).

For imaging, a Zeiss XRM-510 X-ray computed tomography scanner was employed. The X-ray detector assembly of objective 0.4X was used, and the X-ray energy was set at 80 keV, with a power output of 7 W. Each scan had an exposure time of 2 s and a total of 3201 projections, resulting in a scanning duration of approximately 4 h. The arrangement of the X-ray source, sample, and X-ray detector was configured to achieve an image with a voxel size of 4 µm. Given the 3D image size of approximately 2000 × 2000 × 2000, each scan covered a volume of approximately 8 × 8 × 8 mm^3. To capture the entire 24 mm length of the sample, a total of 4 scans were performed along the sample's length, with an overlap of 1.6 mm at both the bottom and top of the sample. This overlap facilitated the stitching of the individual scans into a single cohesive 3D image for subsequent image processing. The micro-CT scanning locations are illustrated in Fig. 2.

The sample was encased in a Viton sleeve and placed inside a carbon fiber Hassler-type core holder. A 6-mm diameter water-wet porous plate, with a thickness of 5 mm and a mean pore size of 0.08 microns, corresponding to an entry pressure of 3.55 MPa, was positioned at the outlet. This water-wet porous plate served as a barrier to oil during drainage, preventing oil from flowing through it as long as the pressure difference remains below the entry pressure. During oil injection, the pressure difference increased, allowing oil to displace brine from the pore space and push it through the water-wet porous plate. To control the flow rate and pressure, four high-pressure syringe pumps (Teledyne D-Series Pumps) were used: One pump maintained the confining pressure of the core holder, another regulated the back pressure, while the remaining two pumps injected oil or brine into the sample. All flow lines were assembled using 1/16-inch (1.6 mm) polyether ether ketone (PEEK) tubing, which is chemically inert. The pressure difference was monitored using a

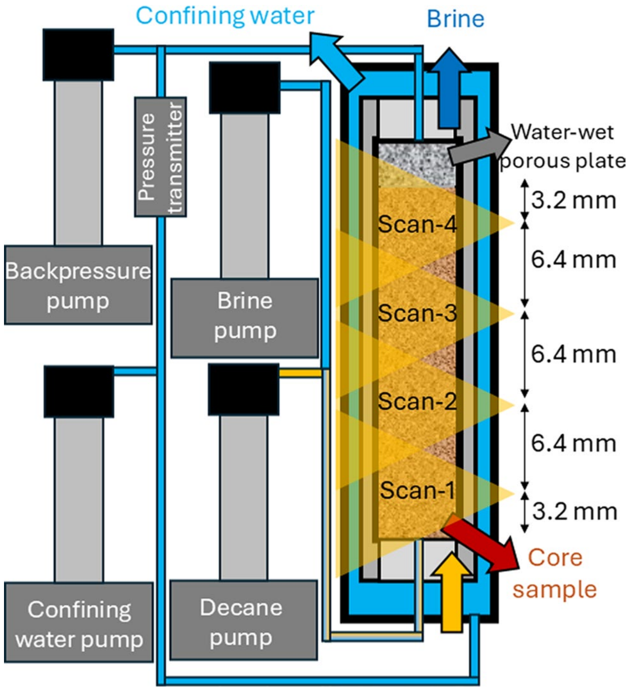

Fig. 2 The experimental apparatus using a Hassler-type core holder, a water-wet porous plate, a pressure transmitter, four high-pressure syringe pumps, and a micro-CT scanner with the four vertical locations used for imaging

Keller PD-33X series pressure transmitter, which has a pressure range of 0 to 5 MPa. The overall schematic of the apparatus is illustrated in Fig. 2.

2.2 Experimental Methods

The step-by-step procedure was as follows:

1. A confining pressure of 2000 kPa above the backpressure and injection pressure was always applied and maintained within the core holder to compress the Viton sleeve around the sample, preventing fluid bypass.
2. The sample containing only air was then imaged, resulting in a dry scan.
3. CO_2 gas was injected into the sample to displace air, and then the sample was vacuumed to remove the remaining CO_2. Any CO_2 remaining in the sample after vacuuming will dissolve in the brine, ensuring complete saturation.
4. Brine was then injected into the sample at 5000 kPa pressure difference for several hours, corresponding to 100 pore volumes (PV) to ensure complete brine saturation. This high pressure was required since the water-wet porous plate had a low permeability of approximately 1.8 μD obtained from measuring the pressure difference during this process.
5. This brine-saturated sample was imaged, resulting in the brine-saturated scan.

6. Afterward, the drainage experiment was started by injecting decane at elevated pressures difference of 10, 50, 200, 1000, 2000, and 3000 kPa. For each scan, pressure was maintained at least for 24 h before changing the pressure to ensure sufficient time to reach equilibrium for each scan. Throughout the experiments, pressure fluctuations of about ± 9 kPa with a period of around 24 h were observed. This fluctuations did not come from the pressure transducer uncertainty but could be the response of the system with the porous plate.

2.3 Image Processing and Data Analysis

The 3D images from four different scanning locations were stitched together to create a cohesive 3D image. To ensure uniform brightness and contrast across the images, normalization of the gray scale values was conducted using the Viton sleeve and confining water as references for adjusting brightness and contrast, as illustrated in Figure 3a. As shown in Fig. 3b, the gray values of the sleeve (green) and confining water (blue) at lengths 2 and 4 differed significantly, likely due to mineral impurities with high X-ray absorption at those locations. After normalization, the image was successfully normalized along the entire length, as indicated by the similar gray value of the sleeve (dark green) and confining water (dark blue lines) along the sample. Subsequently, 3D image registration was performed using the bottom image as the anchor for the registration positions. After stitching, a 3D image of 2000 × 2000 × 5000 voxels, corresponding to a physical size of 8 × 8 × 20 mm^3, was obtained. This process was applied to all images captured during various conditions, including dry scans, brine-saturated scans, and scans at pressures of 10 kPa, 50 kPa, 200 kPa, 1000 kPa, 2000 kPa, and 3000 kPa.

After stitching, further registration and normalization still need to be performed again from all the images to register and normalize the images from different scans. Registration was performed by anchoring to the dry images, and normalization again used the Viton sleeve and confining water as the guides with the dry images as the anchor. As the final step before differential imaging, a non-local means filter was applied to remove the noise but still preserve the edges (Buades et al. 2007). As shown in Fig. 3c, the gray scale value histogram after filtering is more concentrated at the peaks, indicating lower standard deviation due to effective noise removal.

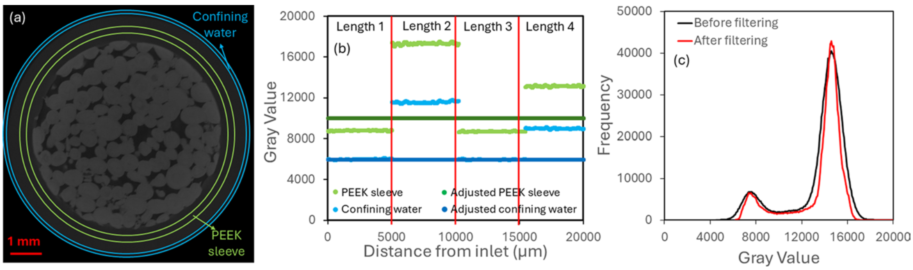

Fig. 3 **a** A two-dimensional cross-section of a three-dimensional image from the dry scan with black and gray as void and solid, whereas the blue and green lines are the Viton sleeve and confining water as the guidance for gray scale value normalization. **b** The gray scale value of the Viton sleeve and confining water in four scanning positions before and after normalization. **c** The gray value histogram before and after filtering

Differential imaging was then performed by subtracting the dry from the wet images, as illustrated in Figs. 4a–c. Subtracting the dry scan from the brine-saturated image produces a differential image representing the porosity distribution, whereas subtracting the dry scan from any image during drainage generates a differential image representing the brine fraction distribution at the given pressure difference. In addition, the brine saturation can also be measured from the porosity and brine fraction. Porosity, brine fraction, and brine saturation are expressed mathematically as follows:

$$\phi = \frac{V_{\mathrm{void}}}{V_{\mathrm{tot}}} \tag{1}$$

$$\delta_{\mathrm{bri}} = \frac{V_{\mathrm{bri}}}{V_{\mathrm{tot}}} \tag{2}$$

$$S_{\mathrm{bri}} = \frac{V_{\mathrm{bri}}}{V_{\mathrm{void}}} = \frac{\delta_{\mathrm{bri}}}{\phi} \tag{3}$$

with V as volume, ϕ as porosity, δ as fluid fraction, S as saturation, and subscripts *tot*, *bri*, and *void* as total, brine, and void, respectively.

The generated differential images, however, still require segmentation into resolved pores, unresolved pores, and solid, as shown in Fig. 4d, indicated by the blue, red, and gray regions, respectively. For gray values above the resolved threshold, the brine fraction is set

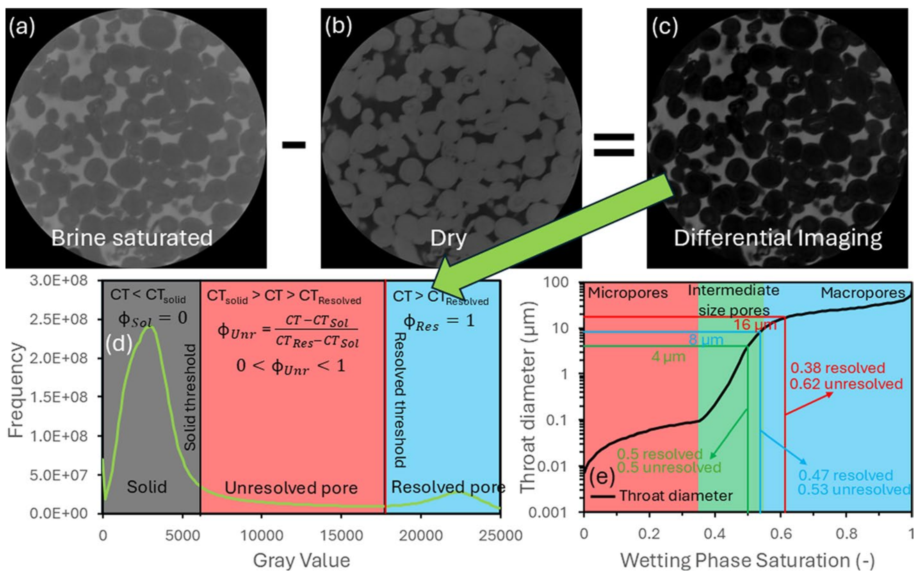

Fig. 4 Example images of **a** the brine-saturated scan, **b** the dry scan, and **c** the differential imaging results. **d** The differential image histogram is divided into resolved pores, unresolved pores, and solid marked as blue, red, and gray regions, respectively. **e** The throat diameter distribution measured from MICP with three classifications of macropores (blue background), intermediate pores (green background), and micropores (red background). In addition, the lines correspond to the threshold guidance based on minimum throat diameter of 4, 8, and 16 μm are also given, respectively, by green, blue, and red lines

to one, while for gray values below the solid threshold, the brine fraction is set to zero. For gray values that fall between the solid and resolved thresholds, the brine fraction varies linearly: Gray values closer to the solid threshold yield a low brine fraction, whereas those closer to the resolved threshold result in a high brine fraction (Akin and Kovscek 2003). These conditions can be expressed mathematically as follows:

$$\delta_{\mathrm{bri,sol}} = 0 \quad \text{for} \quad \mathrm{CT} < \mathrm{CT}_{\mathrm{sol}} \tag{4}$$

$$\delta_{\mathrm{bri,res}} = 1 \quad \text{for} \quad \mathrm{CT}_{res} < \mathrm{CT} \tag{5}$$

$$\delta_{\mathrm{bri,unr}} = \frac{\mathrm{CT} - \mathrm{CT}_{\mathrm{sol}}}{CT_{\mathrm{res}} - \mathrm{CT}_{\mathrm{sol}}} \quad \text{with} \quad 0 < \phi_{\mathrm{unr}} < 1 \quad \text{for} \quad \mathrm{CT}_{\mathrm{sol}} < \mathrm{CT} < \mathrm{CT}_{\mathrm{res}} \tag{6}$$

with *CT* as the gray value, and the subscripts *res* and *unr* correspond to resolved, and unresolved, respectively. When the brine-saturated image is used, δ_{bri} becomes ϕ since the calculation results in the porosity distribution.

Since selecting thresholds for segmentation can be subjective, we used porosity data from the helium porosimetry and derived throat diameter data from MICP (Tanino and Blunt 2012) (Fig. 4e) as guides. First, the total porosity from the thresholding should match the helium porosimeter data. Second, the ratio of resolved-to-unresolved porosity should align with the MICP data. By following the distribution of throat diameter, the ratio of resolved-to-unresolved porosity can be selected based on the assumption of the smallest throat diameter at the given voxel size.

In this work, for example, the voxel size from micro-CT is 4 µm, and the pore-to-throat size ratio in Ketton limestone is 1.5 (Tanino and Blunt 2012). Therefore, given that the smallest pore identified through image processing is generally three voxels in diameter or larger (Dong and Blunt 2009; Patmonoaji et al. 2020), we assumed the smallest resolved pore size to be 12 µm. Considering the pore-to-throat size ratio in Ketton limestone, the smallest throat diameter is estimated to be 8 µm. This throat size in the MICP data corresponds to a ratio of 0.47 for resolved porosity and 0.53 for unresolved porosity. As a result, the threshold values for solid ($\mathrm{CT}_{\mathrm{sol}}$) and resolved pores ($\mathrm{CT}_{\mathrm{res}}$) were adjusted to match the total porosity from the helium porosimeter and the ratio of resolved-to-unresolved porosity corresponding to the smallest throat diameter from MICP.

This method can then be applied to measure the brine fraction from all drainage data using the same thresholds. However, since the dry images contain gas and solid, while the drainage images contain oil, brine, and solid, there is a difference in the gray value between gas and oil. Oil has a higher gray value than gas due to its greater density. As a result, when calculating the brine fraction distribution, the solid threshold value is adjusted by adding this gray value difference to account for the presence of oil.

For sensitivity analysis and error estimation, other assumptions for throat sizes of 4 µm and 16 µm were also considered, as shown by the green and red lines, respectively. The assumption of a 4 µm throat size yielded a resolved-to-unresolved porosity ratio of 0.5 to 0.5, while considering 16 µm gave a ratio of 0.38 to 0.62.

This porosity map is also used to distinguish between micro-, intermediate-, and macropores. The classification is based on masks derived from the porosity distribution, where a porosity value of one represents macropores, values below 0.25 correspond to micropores, and intermediate-size pores fall within the remaining range. As a result, the brine fraction in each category can be quantified.

3 Results and Discussion

3.1 Porosity Map

Axial images from the dry scan and brine-saturated scan are shown in Fig. 5a and b, where dark represents void, gray represents solid, and bright represents brine. Although intermediate-size pores are distributed throughout the sample, more intermediate-size pores can be observed within the green circle, located between 8 mm and 18 mm from the inlet. Aside from this localized intermediate pore accumulation, the porous media structure appears to be generally homogeneous, demonstrated by the uniform ooid size and distribution.

After processing with differential imaging, image segmentation was performed distinguishing three categories: solid (black), unresolved pores (red), and resolved pores (blue), as shown in Fig. 5c. This segmentation was based on the threshold values from equations 4-6. In the region of the green circle, which represents the accumulation of intermediate-size pores, no resolved pores were observed. In contrast, in other regions, resolved pores are uniformly distributed, corresponding to the intergranular packing of the ooids.

By assigning the porosity values from equations 4-6, a porosity map was generated, as shown in Fig. 5d. In the porosity map, resolved pores are white (porosity equal to one), solid is shown in black (porosity equal to zero), and unresolved pores are represented by the remaining colors. The porosity distribution for intermediate-size pores is present in both resolved and unresolved pores, as interstitial particles can sparsely fill the intergranular spaces, creating relatively larger pore sizes. This results in a wide porosity range, between 0.2 and 1. Consistent with Fig. 5c, no resolved pores are observed in the green circle due to the accumulation of intermediate-size pores in that region. The porosity

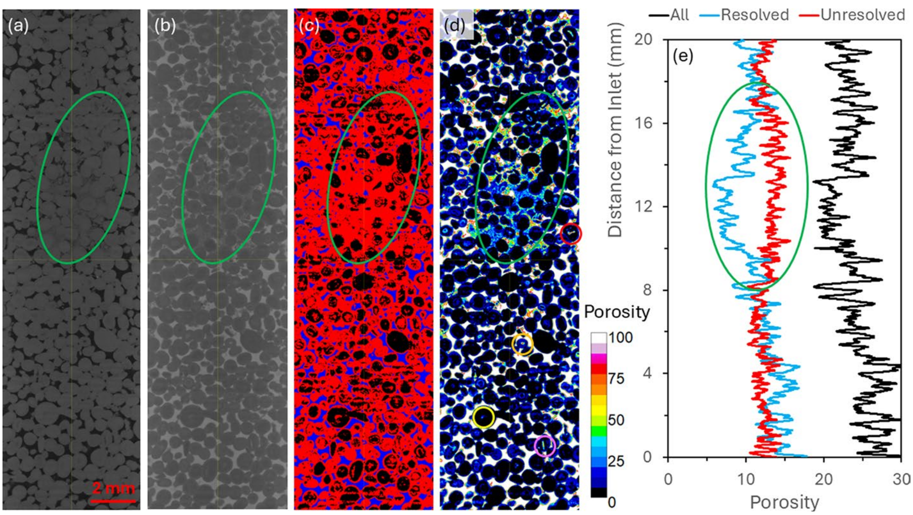

Fig. 5 Axial cut of **a** the dry scan, **b** brine-saturated scan, and **c** segmented images into three categories (black as solid, red as unresolved pore, and blue as resolved pore). **d** Porosity map as shown by the color bar and the red, orange, yellow, and pink circles focusing on ooids with higher porosity in the center. **e** Porosity distribution for all, resolved, and unresolved along axis of flow with resolved and unresolved ratio of 0.468 and 0.532, corresponding to a minimum resolved throat size of 8 μm. The green circles focuses on the intermediate pore regions due to accumulation of interstitial particles

distribution of micropores, on the other hand, is confined to the unresolved pores and is located in the radial concentric layers of the ooids, with porosity values ranging from 0.1 to 0.2. However, some ooids show high porosity at their centers, as highlighted by the red, orange, yellow, and pink circles in Fig. 5d. This is possible because the ooid was originally formed from a fragment of shell, sand grain, or other debris before precipitation, as discussed previously. Thus, macropores are represented by the resolved pores, while micropores are represented by the unresolved pores. Intermediate-size pores, however, include both resolved and unresolved pores and are easier to invade than micropores.

The quantitative values of all, resolved, and unresolved porosity are shown in Fig. 5e, as a cross-sectional average along the sample axis. At the location of the green circle (approximately 8 to 18 mm from the inlet), the resolved porosity is lower, while the unresolved porosity is slightly higher, resulting in a lower total porosity. The average total porosity is 0.24, which is consistent with the helium porosimeter measurement of 0.239 ± 0.008, with a resolved-to-unresolved porosity ratio of 0.468 and 0.532, respectively. This ratio closely matches the resolved and unresolved ratio obtained from MICP for a minimum throat diameter of 8 μm, demonstrating consistency with the image processing method described in Sect. 2.

3.2 Brine Fraction Map Throughout Drainage

The axial cut images at various pressure differentials are shown in Fig. 6a–f. At the beginning of oil injection at 10 kPa, decane has already displaced most of the brine from the macropores, leaving brine primarily in the intermediate-size pores and micropores. The brine within the green circle becomes barely visible and continues to fade until 200 kPa, indicating its gradual displacement by oil. Beyond this pressure, up to 3000 kPa, no significant changes are observable in the gray images.

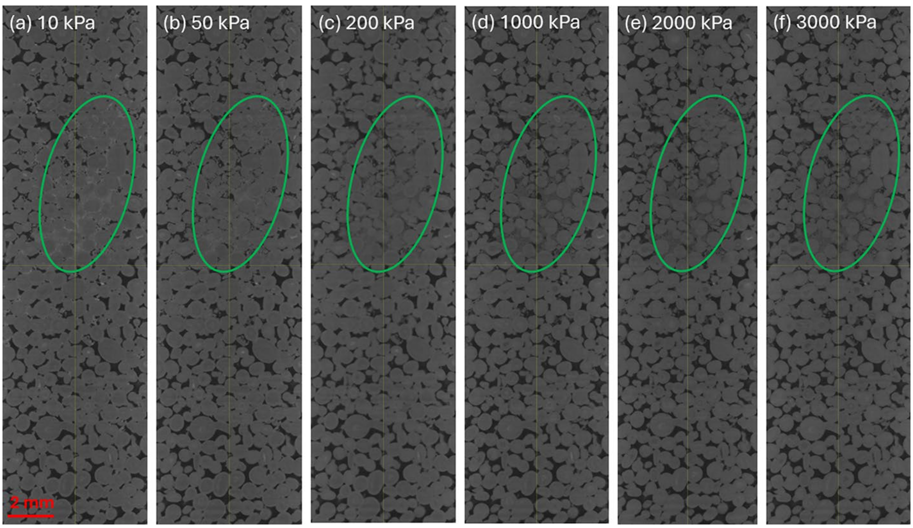

Fig. 6 Axial cut of the images at pressure differences of **a** 10, **b** 50, **c** 200, **d** 1000, **e** 2000, and 3000 kPa

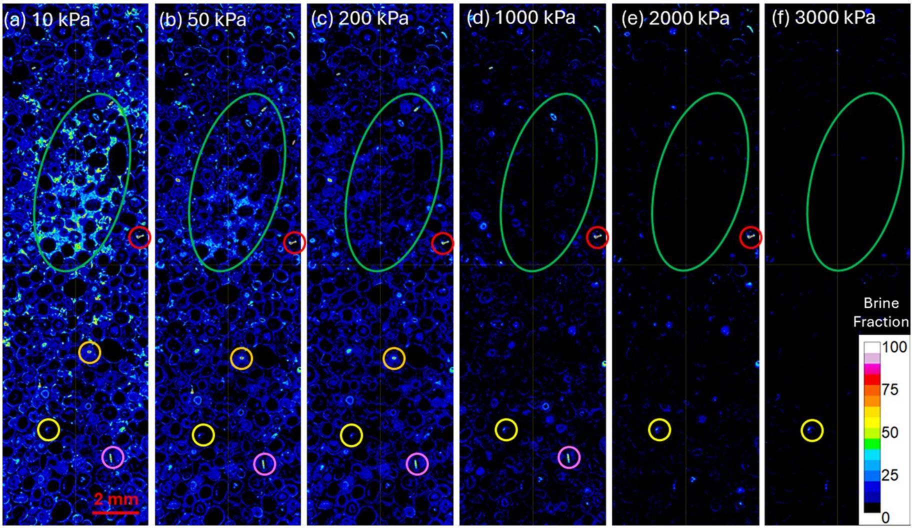

Fig. 7 Axial cut of brine fraction maps at pressure differences of **a** 10, **b** 50, **c** 200, **d** 1000, **e** 2000, and 3000 kPa with the green circles indicating intermediate-size pores, while the red, orange, yellow, and pink circles highlight the porous center of ooids

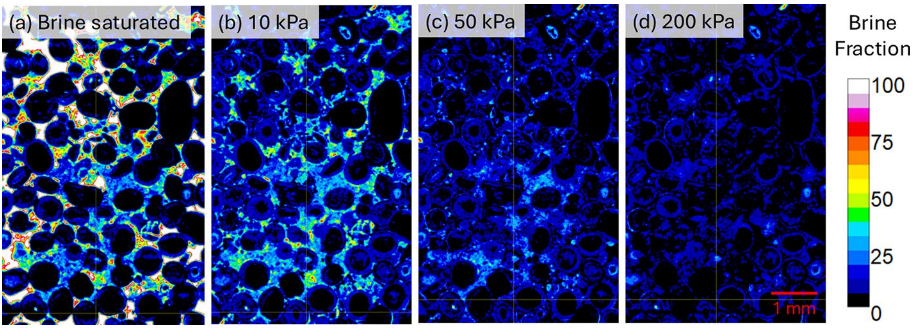

Fig. 8 Axial cut of brine fraction maps focusing on the intermediate-size pores when **a** brine saturated and at the capillary pressure of **b** 10 kPa, **c** 50 kPa, and **d** 200 kPa

In contrast, the brine fraction maps in Fig. 7a–f clearly highlight the brine displacement through color changes. Overall, the brine fraction diminishes as the pressure difference increases, indicating that brine is progressively displaced from the pores and flushed through the porous plate. The green circles highlight the displacement of the accumulated intermediate-size pores, whereas other smaller circles in red, orange, yellow, and pink focus on the displacement of water from the center of ooids with high porosity.

The brine displacement from the intermediate-size pores within the green circle (Fig. 7a–f) was significant up to a pressure difference of 200 kPa. Figure 8a–e provides a closer look at this intermediate-size pore region under pressure differences ranging from 10 kPa to 200 kPa. At the initial brine-saturated condition, brine also occupied the macropores. However, with a slight pressure increase of just 10 kPa, brine was flushed from the macropores, leaving the remaining brine primarily within the intermediate-size pores. As the pressure increased to 50 kPa, brine in the intermediate-size pore region was partially displaced. At 200 kPa, the brine was displaced almost completely from the intermediate-size pores, and thus, the remaining brine is only in the concentric layers of the ooid spheres.

Significant brine displacement in the micropores predominantly occurred after 200 kPa. Interestingly, the displacement within the high-porosity cores (Fig. 7a–f) varied across different pressure levels, ranging from 1000 kPa to no displacement even at 3000 kPa. For instance, the displacement in the red circle occurred after 2000 kPa, whereas the displacement in the orange and pink circles took place after 200 kPa and 1000 kPa, respectively. However, in the yellow circle, brine persisted even at 3000 kPa. This suggests that the high-porosity centers of the ooid spheres can only be accessed via the surrounding micropores of the concentric ooid layers, which require higher pressure differences to penetrate. Figure 9a–e presents the brine fraction maps of an ooid within the orange circle, under brine-saturated conditions and varying pressure differences. Initially, the ooid was surrounded by brine in the macropores, but the brine was rapidly displaced at just 10 kPa. No significant changes were observed until 200 kPa, after which the brine within the ooid was finally displaced at 1000 kPa.

The brine saturation in resolved pores, unresolved pores, and all pores during drainage is illustrated in Fig. 10. Most of the brine fraction in resolved pores was displaced early at 10 kPa, resulting in near-zero resolved saturation along the sample. Conversely, the brine saturation in unresolved pores decreased with increasing pressure difference, indicating displacement of brine by oil. Overall, the brine saturation distribution along flow direction remained relatively homogeneous throughout drainage, except at the initial stages at 10 kPa and 50 kPa. Higher brine saturation was observed at the inlet distance of 10 to 14 mm, corresponding to brine accumulation in the intermediate-size pores. For the remaining pressures, where most of the brine was located within the ooid spheres, saturation tended to be uniform, suggesting

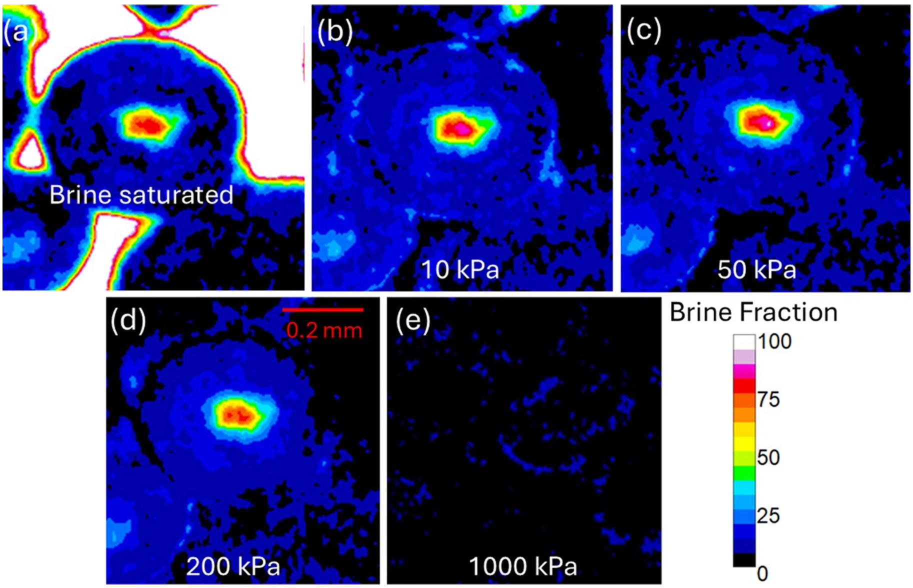

Fig. 9 Brine fraction maps focusing on an ooid sphere when **a** brine saturated and at the capillary pressure of **b** 10 kPa, **c** 50 kPa, and **d** 200 kPa, and **e** 1000 kPa

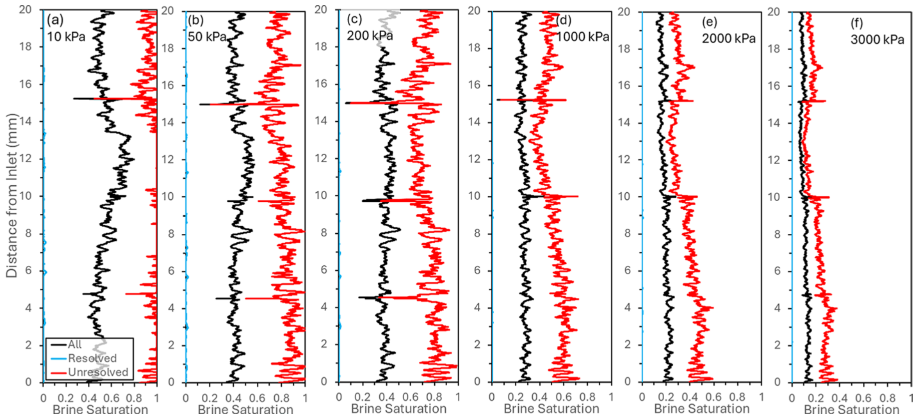

Fig. 10 The cross-sectional average of brine saturation in resolved pores (blue line), unresolved pores (red line), and all pores (black line) throughout drainage

uniform brine distribution in the ooid spheres. By the end of drainage at 3000 kPa, not all brine had been displaced by oil with residual brine located in the ooid spheres.

3.3 Capillary Pressure

Figure 11 presents the average brine saturation across the entire sample at various capillary pressures. The brine saturation is divided into three categories: resolved pores (blue line), unresolved pores (red line), and all pores (gray line). For comparison, the MICP adjusted decane–brine system is also included (black line). The adjustment of the MICP was made using the fluid parameter ratio, based the Young–Laplace equation, as follows:

$$P_{c,\text{dec/bri}} = \frac{\sigma_{\text{dec/bri}} \cos\theta_{\text{dec/bri}}}{\sigma_{\text{mer/vac}} \cos\theta_{\text{mer/vac}}} P_{c,\text{mer/vac}} \tag{7}$$

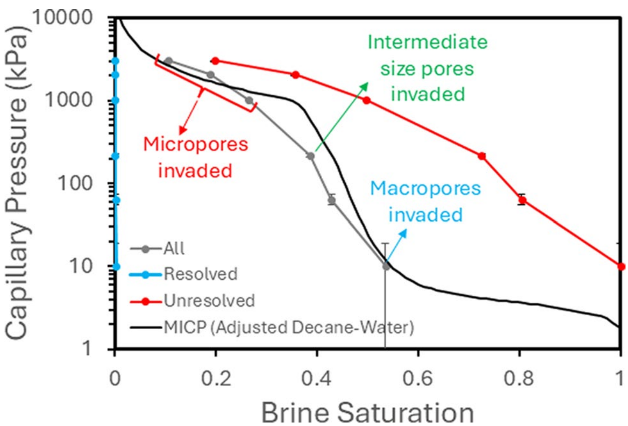

Fig. 11 The capillary pressure as a function of brine saturation in resolved pores (blue line), unresolved pores (red line), all pores (gray line), and MICP adjusted to decane and water from equation 7 (black line)

with P_c as capillary pressure, σ as interfacial tension, θ as contact angle, and the subscripts *dec*, *mer*, and *vac* are decane, mercury, and vacuum, respectively. $\sigma_{\text{mer/vac}}$ is taken as 0.48 N/m. $\theta_{\text{dec/bri}}$ and $\theta_{\text{mer/vac}}$ are assumed to be 20 (Duffy et al. 2021) and 140 degrees (Ellison et al. 1967; Darling 2005; Good 1981), respectively.

Consistent with the imaging results, brine in the macropores is displaced almost immediately, leading to near-zero resolved pore saturation throughout drainage. In contrast, the brine saturation in unresolved pores gradually decreases as the pressure difference increases. As a result, the overall brine saturation declines mainly due to the displacement of brine from unresolved pores. The imaging data shows that at 10 kPa, the macropores were already drained, and by 200 kPa, the intermediate-size pores were mostly invaded. At higher pressure differences, up to 3000 kPa, the remaining brine was still being displaced from the micropores, as indicated in Fig. 11.

The gradient of the capillary pressure function is also consistent with the MICP data. However, due to pressure fluctuations of 9 kPa, measurements below 10 kPa are not available, leading to the observation of only two distinct gradients. Between pressure differences of 10, 50, and 200 kPa, the reduction in brine saturation with increasing pressure is less pronounced compared to the higher pressure differences of 1000, 2000, and 3000 kPa. This shift in gradient reflects the transition from brine displacement in the intermediate-size pores to that in the micropores.

The capillary pressure function for each pore size category is shown in Fig. 12. This measurement was performed using masks derived from the porosity distribution, where porosity values of one represent macropores, values below 0.25 represent micropores, and the intermediate-size pores fall within the remaining range. Consistent with the resolved pore observations in Fig. 11, macropores are fully drained at a capillary pressure of 10 kPa. Micropores were accessed at pressures above 1000 kPa. Intermediate-size pores, however, show the most significant saturation drop at 1000 kPa or less, with some saturation persisting even at 3000 kPa. Since the intermediate pore region is identified by selecting areas with porosity values between 0.25 and 1.0, this category also includes the high-porosity regions within ooids. Consequently, substantial brine displacement occurs as ooid intrusion begins, and residual saturation remains at higher pressures due to the need for a

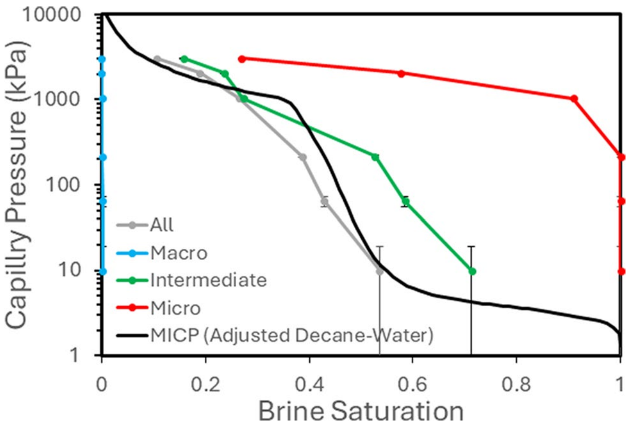

Fig. 12 The capillary pressure as a function of brine saturation in all pores (gray line), macropores (blue line), intermediate-size pores (green line), micropores (red line), and MICP adjusted to decane and water from equation 7 (black line)

high-pressure difference to displace brine from within the ooids. Thus, at high capillary pressure, intermediate-sized pores continue to be accessed with micropores due to fluid displacement from the ooid centers.

To check the uncertainty and sensitivity of the DIPP results, the capillary pressure measured by assuming a minimum resolved throat diameter of 4, 8, and 16 μm is given in Fig. 13. The vertical uncertainty is due to local pressure fluctuations of approximately 9 kPa. Since this fluctuation is constant, it only shows significant effect at low-pressure difference.

As shown in Fig. 13, the measurement with DIPP demonstrates overall lower brine saturation than MICP at the same capillary pressure, or a lower capillary pressure for the same saturation. This difference can likely be attributed to the nature of MICP measurements. Since mercury in a vacuum is used to represent the fluid pair, there is no irreducible saturation. Additionally, the rapid measurement process of MICP may not allow sufficient time for mercury to fully penetrate pores, particularly smaller ones.

In laminated sandstone, capillary pressure measured using DIPP was also lower than MICP (Lin et al. 2017), confirming that the lower capillary pressure observed in DIPP is not merely a phenomenological effect of the porous media structure. Since the fluid pair of interest is used, these findings suggest that employing fluid-based methods alongside porous plate techniques provides a more representative assessment of capillary pressure and pore structure in multiscale porous media compared to MICP.

4 Conclusions

We classified the pores in Ketton limestone into three categories: macropores, intermediate-size pores, and micropores, based on geological insights, micro-CT imaging, MICP measurements, and SEM analysis. Macropores are formed by the intergranular packing of ooids, micropores are attributed to the intragranular porosity within the ooids, and intermediate-size pores arise from interstitial particles filling the macropores. This classification is further supported by fluid distribution observations during drainage using DIPP, where

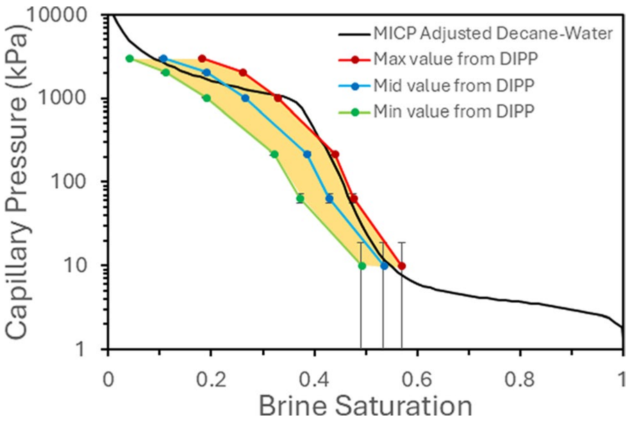

Fig. 13 The capillary pressure function for drainage measured with different assumed minimum resolvable throat diameters of 4, 8, and 16 μm, representing the minimum (green line), mid-range (blue line), and maximum (red line) values, respectively. MICP adjusted decane–water is also given as comparison (black line)

displacement occurred progressively from the largest to the smallest pore sizes: from the intergranular packing, to interstitial particles, and finally to the intragranular ooid pores.

We improved the DIPP method by incorporating helium porosimetry, MICP, and micro-CT voxel size to determine threshold values for unresolved and resolved porosity. Helium porosimetry served as the anchor for total porosity, while MICP and micro-CT voxel size guided the ratio of unresolved-to-resolved porosity based on the assumed minimum identifiable pore diameter. Uncertainty bounds derived from this method can be assessed by varying the minimum identified pore diameter.

The capillary pressure was compared with MICP, revealing that DIPP results generally exhibit lower values. This trend is consistent with previous findings by Lin et al. (2017) for laminated samples, indicating that it is not merely a phenomenological effect of the porous media structure. This study suggests that for complex porous media with a wide pore size distribution, combining imaging with a porous plate for capillary pressure measurements offers a more reliable and accurate approach. This method allows the use of the fluid pair of interest while enabling spatial monitoring of fluid distribution across different pore sizes.

This method presents an alternative approach to capillary pressure measurement using digital rock physics technology, complementing conventional measurement techniques such as MICP, porous plate, and centrifuge. With DIPP, spatial fluid distribution can be monitored throughout the capillary pressure measurement, offering pore-scale insights into the location of trapped oil or contaminants at a given capillary pressure. As a result, effective injection strategies can be designed based on better-informed decisions.

Future work could extend this method to a wider range of samples, and be applied using a hydrophobic (oil-wet) porous plate to study imbibition and waterflooding.

Acknowledgements We gratefully acknowledge TotalEnergies for providing financial support and for helpful discussion and comments on this work with their digital rock physics team.

Author Contributions Conception and design were performed by all authors. Experimental investigation was performed by AP and RC. The image processing and data analysis were performed by AP and ASG. The supervision of the work were conducted by MJB and BB. Original draft writing was performed by AP. All authors contributed to the edit and review.

Funding This work is funded by TotalEnergies.

Declarations

Conflict of interest The authors declare that they have no conflict of interest.

References

Akin, S., Kovscek, A.R.: Computed tomography in petroleum engineering research. J. Geol. Soc. **215**, 23–38 (2003)

Andersen, P.: Capillary pressure effects on estimating the enhanced-oil-recovery potential during low-salinity and smart waterflooding. Soc. Petrol. Eng. J. **25**(1), 481–496 (2020)

Ayappa, K.G., Davis, H.T., Davis, E.A., et al.: Capillary pressure: centrifuge method revisited. Am. Inst. Chem. Eng. J. **35**(3), 365–372 (1989)
Bashir, A., Ali, M., Patil, S., et al.: Application of ozone micro-nano-bubbles to groundwater remediation. J. Hazard. Mater. **342**, 446–453 (2018)
Batchelor, M.T., Burne, R.V., Henry, B.I., et al.: A biofilm and organomineralisation model for the growth and limiting size of ooids. Sci. Rep. **8**, 559 (2018)
Bear, J.: Dynamics of Fluids in Porous Media. Dover, Garden city (1972)
Blunt, M.J.: Multiphase Flow in Permeable Media: A Pore-Scale Perspective. Cambridge University Press, Cambridge (2017)
Bruckmann, F.E.: Specimen physicum exhibens historam naturalem Oolithi, Helmestadii Salomonis Schnorri (1721)
Buades, A., Coll, B., Morel, J.M.: Nonlocal image and movie denoising. Int. J. Comput. Vis. **76**, 123–139 (2007)
Cheng, H., Wang, F., Yang, G., et al.: Prediction of relative permeability from capillary pressure based on the fractal capillary bundle model. Appl. Thermal Eng. **239**, 122093 (2024)
Coogan, A.H.: Measurements of compaction in oolitic grainstone. J. Sediment. Petrol. **40**(3), 921–929 (1970)
Darling, T.: Well Logging and Formation Evaluation (Gulf Drilling Guides). Gulf Professional Publishing, Houston (2005)
Diaz, M.R., Eberli, G.P.: Decoding the mechanism of formation in marine ooids: a review. Earth Sci. Rev. **190**, 536–556 (2019)
Dong, H., Blunt, M.J.: Pore-network extraction from micro-computerized-tomography images. Phys. Rev. E **80**, 036307 (2009)
Duffy, T.S., Li, J., Johns, R.T., et al.: Capillary contact angle for the quartz-distilled water-normal decane interface at temperatures up to 200 °c. Colloids Surfaces A Physicochem. Eng. Aspects **609**, 125608 (2021)
Ellison, A.H., Klemm, R.B., Schwartz, A.M., et al.: Contact angles of mercury on various surfaces and the effect of temperature. J. Chem. Eng. Data **12**(4), 607–609 (1967)
Falode, O., Manuel, E.: Wettability effects on capillary pressure, relative permeability, and irredcucible saturation using porous plate. J. Petrol. Eng. **2014**(1), 465418 (2014)
Good, R.J.: The contact angle in mercury intrusion porosimetry. Powder Technol. **29**(1), 53–62 (1981)
Harris, P.M., Diaz, M.R., et al.: The formation and distribution of modern ooids on Great Bahama Bank. Ann. Rev. Mar. Sci. **11**, 491–516 (2019)
Heinemann, N., Alcalde, J., Miocic, J.M., et al.: Enabling large-scale hydrogen storage in porous media—the scientific challenges. Energy Environ. Sci. **14**, 853–864 (2021)
Hu, L., Xia, Z.: Application of ozone micro-nano-bubbles to groundwater remediation. J. Hazard. Mater. **342**, 446–453 (2018)
Hudson, J., Clements, R.: The middle jurassic succession at Ketton, Rutland. Proc. Geol. Assoc. **118**(3), 239–264 (2007)
Jiao, L., Østebø Andersen, P., Zhou, J., et al.: Applications of mercury intrusion capillary pressure for pore structures: a review. Capillarity **3**(3), 62–74 (2020)
Jo, Y.J., Lee, J.Y., Yi, M.J., et al.: Soil contamination with TCE in an industrial complex: contamination levels and implication for groundwater contamination. Geosci. J. **14**(10), 313–320 (2010)
Lin, Q., Al-Khulaifi, Y., Blunt, M.J., et al.: Quantification of sub-resolution porosity in carbonate rocks by applying high-salinity contrast brine using x-ray microtomography differential imaging. Adv. Water Resources **96**, 306–322 (2016)
Lin, Q., Bijeljic, B., Rieke, H., et al.: Visualization and quantification of capillary drainage in the pore space of laminated sandstone by a porous plate method using differential imaging x-ray microtomography. Water Resources Res. **53**(8), 7457–7468 (2017)
Lin, Q., Bijeljic, B., Raeini, A.Q., et al.: Drainage capillary pressure distribution and fluid displacement in a heterogeneous laminated sandstone. Geophys. Res. Lett. **48**(14), e2021GL093604 (2021)
Patmonoaji, A., Tsuji, K., Suekane, T.: Pore-throat characterization of unconsolidated porous media using watershed-segmentation algorithm. Powder Technol. **362**, 635–644 (2020)
Patmonoaji, A., Hu, Y., Nasir, M., et al.: Effects of dissolution fingering on mass transfer rate in three-dimensional porous media. Water Resources Res. **57**(10), e2020WR029353 (2021)
Porter, M.L., Wildenschild, D., Grant, G., et al.: Measurement and prediction of the relationship between capillary pressure, saturation, and interfacial area in a NAPL-water-glass bead system. Water Resources Res. **46**(8), W08512 (2010)
Tanino, Y., Blunt, M.J.: Capillary trapping in sandstones and carbonates: dependence on pore structure. Water Resources Res. **48**(8), W08525 (2012)
Vavra, C.L., Kaldi, J.G., Sneider, R.M.: Geological applications of capillary pressure: a review. Am. Assoc. Petrol. Geol. Bull. **76**(6), 840–850 (1992)

Zhang, G., Regaieg, M., Blunt, M.J., et al.: Primary drainage and waterflood capillary pressures and fluid displacement in a mixed-wet microporous reservoir carbonate. J. Hydrol. **625**, 130022 (2023)